Taylor & Francis
Taylor & Francis Group

Design optimization of a hydraulic flywheel accumulator for a hydraulic hybrid vehicle

Kyle G. Strohmaier, Paul M. Cronk and James D. Van de Ven*

Department of Mechanical Engineering, University of Minnesota, 111 Church St SE, Minneapolis, MN 55455, USA

The hydraulic flywheel accumulator is a novel energy storage device that has the potential to overcome major drawbacks of conventional energy storage methods for mobile hydraulic systems. By employing a rotating pressure vessel, the hydraulic flywheel accumulator stores energy in both the hydro-pneumatic domain and the rotating kinetic domain. This allows for energy storage densities many times higher than conventional hydraulic accumulators and adds a degree of freedom that decouples state of charge from the hydraulic system pressure. This paper summarizes various mechanical stress and energy models developed to describe the behavior of the hydraulic flywheel accumulator. The models are used in an example design optimization to illustrate the utility of the hydraulic flywheel accumulator. The resulting design solution delivers an energy storage density at least six times greater than traditional composite hydraulic accumulators while exhibiting efficiencies above 75%.

Keywords: hydraulic flywheel accumulator; kinetic energy storage; hydraulic energy storage; HFA; dual energy storage domain

1. Introduction

1.1. Transportation emissions and existing vehicle technology

The advent of hybrid vehicles has increased the energy efficiency of the transportation industry (Environmental Protection Agency 2015). Among passenger hybrid vehicles, integration of electric powertrain components is the most common means of hybridization. However, hydraulic components offer significantly higher power density and durability (Filipi *et al.* 2004) and are far less expensive to manufacture.

The traditional means of storing hydraulic energy is with a hydro-pneumatic accumulator, a pressure vessel in which a bladder, diaphragm, or piston separates the hydraulic fluid from a pre-charged gas. Even using the highest-performance materials, the energy density of the best accumulators today is about 6 kJ/kg (Pourmovahed *et al.* 1988), which is two orders of magnitude lower than present Li-Ion battery technology. This represents a difficult barrier to the viability of hydraulics in hybrid vehicle powertrains. An additional drawback of traditional hydraulic energy storage is the coupling between pressure and state-of-charge (SOC). To meet vehicle power demands at the low system pressures that occur at low states of charge, hydraulic pumps and motors must be oversized, adding both mass and cost to the hydraulic system.

Much of the past research on traditional hydraulic accumulators has focused on optimizing the efficiency of the gas compression process. Several methods have been proposed to improve the convection coefficient between the gas and the outside environment (Perkins 1973, Pourmovahed *et al.* 1988). While these methods have shown some success, they offer only incremental improvements to hydraulic energy storage. Li *et al.* have addressed the two cited drawbacks of hydraulic energy storage by adding an air compressor to form an open accumulator (Li *et al.* 2007). The main challenges with the open accumulator arise from the large amount of convective heat transfer required for near-isothermal (i.e. efficient) operation. The strain energy accumulator is another novel hydraulic energy storage method (Pedchenko and Barth 2009), but it faces challenges associated with the complex hysteresis effects of elastic materials, as well as the difficulty of gripping a strong, highly-strained material (Tucker and Barth 2013).

1.2. The hydraulic flywheel-accumulator approach

The hydraulic flywheel-accumulator (HFA) has the potential to overcome both of the drawbacks of a traditional hydraulic accumulator, significantly increasing energy storage density while decoupling system pressure from SOC (Van de Ven 2009). In the most basic sense, the HFA is a piston-type accumulator that is spun about its longitudinal axis. As in a traditional accumulator, hydro-pneumatic energy can be added or extracted via the addition or extraction of oil through a port. A high-speed rotary union (HSRU) facilitates this exchange of oil between the rotating HFA and the static environment. A hydraulic pump/motor (PM) coupled to the gas side of the HFA manipulates the rotational energy by applying a positive or negative torque. This unit will be referred to

---

*Corresponding author. Email: vandeven@umn.edu

as the "storage PM" to differentiate from the "traction PM" that applies torque to the vehicle's axle.

Kinetic energy is stored in the HFA by virtue of its rotation and the combined moment of inertia of the solid container and the internal fluid. Previous work suggests that the employment of the kinetic energy domain can increase energy storage density by an order of magnitude over traditional accumulator storage (Van de Ven 2009). In addition to increasing energy density, rotation generates a radially dependent parabolic pressure distribution in the hydraulic oil (Van de Ven 2009), which can be described by the following equation:

$$P_o(r) = P_s + \frac{1}{2}\rho_o\omega^2 r^2 \qquad (1)$$

where P_o is oil pressure at radial position r, P_s is system pressure, ρ_o is oil density, and ω is the angular velocity of the HFA. As the position of the port coincides with the radial position $r = 0$, the rest of the hydraulic system experiences a pressure that is lower than the average HFA pressure. This average pressure indicates the amount of stored pneumatic energy. An isothermal compression model is used for the gas, which is reasonable if a heat transfer medium is implemented in the gas volume (Pourmovahed *et al.* 1988). This results in the following expression for the usable pneumatic energy:

$$E_p = P_c V_c \ln\left(\frac{V_c}{V_g}\right) \qquad (2)$$

where E_p is the pneumatic energy, P_c is the charge pressure of the gas at minimum oil volume, V_c is the volume of the gas at minimum oil volume, and V_g is the instantaneous gas volume.

During steady-state (rigid body rotation of the fluid), the kinetic energy of the HFA is:

$$E_k = \frac{1}{2}\left(I_s + I_f\right)\omega^2 \qquad (3)$$

where E_k is kinetic energy, I_s is the rotational inertia of the solid components, and I_f is the inertia of the fluid component.

The pneumatic and kinetic energy terms add together to yield a total stored energy, E, of:

$$E = E_k + E_p = \frac{1}{2}\left(I_s + I_f\right)\omega^2 + P_c V_c \ln\left(\frac{V_c}{V_g}\right) \qquad (4)$$

Equations (1)–(4) show that the ability to actively control rotational speed via the storage PM adds an additional control variable when compared to a traditional accumulator. This added degree of freedom effectively decouples system pressure from SOC.

Using the preceding pressure and energy equations as a foundation, the remainder of this paper discusses the design choices, some of which are influenced by the need for easy prototyping, and performance capabilities of the hydraulic flywheel accumulator. First, the structural architecture is described and stress models are developed for the various components that constitute the

HFA. Next, models are presented for each of the energy loss mechanisms associated with the operation of the HFA, and a simple control strategy for the device is proposed. The paper concludes by discussing the results of a design optimization for an example HFA application.

2. HFA architecture

A conceptual design for the HFA is shown Figure 1. The main component is the housing, consisting of a composite cylinder and a metallic liner of axial length l_h. The housing acts both as a flywheel rotor, storing the majority of the kinetic energy, and as a mechanism to react fluid pressure in the radial direction. Most of the strength of the housing is provided by the composite, which has an outer radius of r_o. The liner, with inner radius r_i and thickness th_l, facilitates sealing between the housing and other concentric components.

Two end caps fit inside of the housing, concentrically on an axle, and seal against the liner. Split retaining rings nested in counterbores in the end caps and grooves in the axle prevent outward axial movement of the end caps. Fluid pressure within the HFA applies an outward force on the endcaps, allowing torque to be transmitted from the axle through the retainers and to the endcaps through friction. Torque is transmitted from the gas-side endcap to the housing with radial pins, which prevent motion in the axial and tangential directions. The oil-side end cap is constrained to the housing only concentrically, such that the internal pressure does not impose any axial stress on the housing.

The piston, which separates the oil from the gas, has axially-sliding seals at both the axle and the housing. As a linear bearing surface, the smaller diameter of the axle provides much better cocking resistance than does the housing. The gas side of the axle is coupled to the storage PM, which applies a torque, *T*. As shown in Figure 2, the end of the oil side of the axle constitutes part of the HSRU. The section of the axle with the smallest outer diameter protrudes into the HSRU case, forming a non-contacting circumferential seal, the purpose of which is
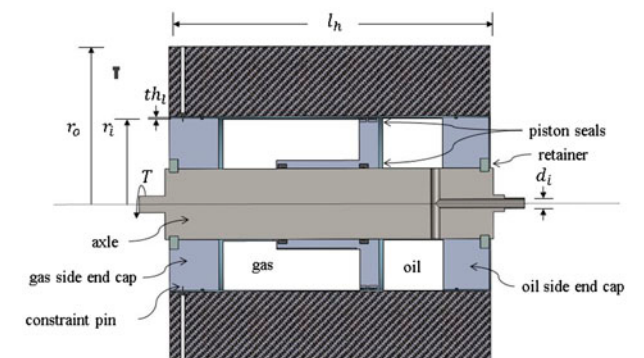

Figure 1. Hydraulic flywheel accumulator architecture with metallic liner and composite wrap.
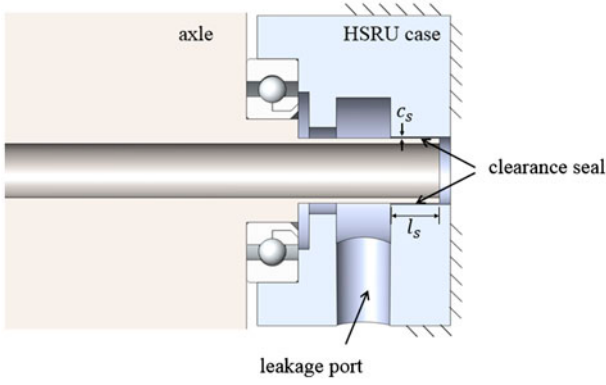
Figure 2. Schematic of the high-speed rotary union concept.

to control leakage without any solid-to-solid contact at the rotating interface.

The HFA is enclosed in a burst containment chamber that is partially voided to provide a vacuum environment, significantly reducing the aerodynamic drag on the rotating components. Since the HSRU exhibits some oil leakage into the vacuum environment, the pressure in the vacuum chamber must remain above the vapor pressure of hydraulic oil, 13 Pa (Exxon Mobil 2008).

3. Model-based structural design

Designing an operable hydraulic flywheel accumulator requires careful consideration of the mechanical stresses in the device. This section describes the stress models that have been developed for each of the components of the HFA.

3.1. Axle

The axial force, F_a, due to fluid pressure on the end caps is the primary load acting on the axle. The axis of rotation is chosen to be vertical, such that the eccentric forces are the only contribution to radial load on the axial and bearings. By placing the HSRU at the bottom, the downward force due to the flywheel mass acts in opposition to the force created by the hydraulic pressure at the HSRU, minimizing the axial bearing stress. To allow for axial strain of the axle and preload the bearings, a wave spring is placed between the gas endcap and upper bearing. Bending of the axle is small, as the bearings are seated directly adjacent to the end caps.

The radial ports in the axle are formed by a single cross-drilled hole, and the length of the axial port is selected such that radial ports enter the HFA just inside the inner face of the oil side end cap. For simplicity, the entire port system has a uniform inner diameter, d_i. All of the remaining axle dimensions are stress-driven and are chosen to minimize the axle mass, since its inertia contribution is sub-optimal (the same amount of mass would provide more inertia if it were concentrated at a

larger radius). The axial force on the axle is expressed as:

$$F_a = \left[P_s + \frac{1}{4}\rho_o\omega^2\left(r_i^2 + r_a^2\right) \right]\pi\left(r_i^2 - r_a^2\right) - k_s\delta_a - m_h g \tag{5}$$

where r_a is the outer axle radius, k_s is the spring constant of the upper bearing retaining spring, δ_a is the axle elongation, m_h is the mass of the housing, and g is acceleration due to gravity. Note that the combined mass of the axle and end caps is neglected, as it is much less than that of the housing. The axial elongation of the axle is a function of its modulus of elasticity, E_a, and axle dimensions, and is expressed as:

$$\delta_a = l_h \frac{F_a}{E_a\pi r_a^2} \tag{6}$$

The axle portion that protrudes into the HSRU is not subject to the axial stress described above. It is modeled in isolation from the rest of the axle and treated as a thick-walled cylinder with free ends. The system pressure P_s acts on the internal wall and the end face while the pressure acting on the external wall is roughly atmospheric. Lamé's equations (Young and Budynas 2002) are used to find the stress at the outer diameter, which is the critical stress location. The wall thickness is selected to withstand the stress at maximum system pressure, with verification that the radial strain keeps the seal clearance in an acceptable range. Because the radius of this portion of the axle is small, torsion due to viscosity in the circumferential seal and centrifugal loading are both neglected. AISI 4340 steel is chosen for the axle material for its high yield strength while gray iron is chosen for the HSRU for its good heat transfer and galling resistance.

3.2. End caps and piston

Like the axle, the end cap mass contributes sub-optimally to the HFA inertia. As such, the optimal end cap thickness, th_e, is that the smallest that allows the end caps to withstand the bending stresses created by the fluid pressure and the stresses imposed by centrifugal force. Stresses due to gravity acting on the masses of the end caps are negligible. The bending and centrifugal forces are evaluated independently and then superimposed to assess the total stress in an end cap.

For a thick-walled cylinder made of an isotropic material exposed to loading only from centrifugal force, the radial, $\sigma_{r,\,cent}$, and circumferential, $\sigma_{c,\,cent}$, stress distributions are functions of radius, r, expressed as (Genta 1985):

$$\sigma_{r,\,cent}(r) = \rho\omega^2 r_o^2\frac{3 + v}{8}\left[1 + \left(\frac{r_i}{r_o}\right)^2 - \left(\frac{r_i}{r_o}\right)^2 - \left(\frac{r}{r_o}\right)^2\right] \tag{7}$$

$$\sigma_{c,\text{cent}}(r) = \rho\omega^2 r_o^2 \frac{3+v}{8}\left[1+\left(\frac{r_i}{r_o}\right)^2+\left(\frac{r_i}{r_o}\right)^2-\frac{1+3v}{3+v}\left(\frac{r}{r_o}\right)^2\right]$$

(8)

where ρ and v are the density and the Poisson ratio of the material, respectively.

The end cap bending stress is modeled using circular plate theory. In this analysis, the retaining ring is presumed to apply a uniform reaction pressure, P_r, over its contact area, and the outer edge of the end cap is assumed to be free of any reaction force or moment. Shear and normal axial stresses are assumed to be zero, and bending stresses on either side of the plate are modeled as equal and opposite (Timoshenko and Woinowsky-Krieger 1959). Methods derived by Heap are used to describe the bending moment profiles in the radial and circumferential directions, M_r and M_c respectively (Heap 1964). Heap defines the bending moments with respect to a circular load W applied at a radius of d on the plate with radial dimensions $b \le r \le a$, with the moments at radii $r < d$ defined

$$M_r = \frac{W}{4\pi}(1+v)\left(1-\frac{b^2}{r^2}\right)\left(\frac{a^2}{a^2-b^2}\right)\left[\frac{1}{2}\left(\frac{1-v}{1+v}\right)\left(1-\frac{d^2}{a^2}\right)+\ln\frac{a}{d}\right]$$

(9)

$$M_c = \frac{W}{4\pi}(1+v)\left(1+\frac{b^2}{r^2}\right)\left(\frac{a^2}{a^2-b^2}\right)\left[\frac{1}{2}\left(\frac{1-v}{1+v}\right)\left(1-\frac{d^2}{a^2}\right)+\ln\frac{a}{d}\right]$$

(10)

and those at radii $r > d$,

$$M_r = \frac{W}{4\pi}(1+v)\left(\frac{a^2}{a^2-b^2}\right)\left[\frac{1}{2}\left(\frac{1-v}{1+v}\right)\left(1-\frac{r^2}{a^2}\right)\left(\frac{d^2}{r^2}-\frac{b^2}{r^2}\right)\right.$$
$$\left.+\ln\frac{a}{r}+\frac{b^2}{a^2}\ln\frac{r}{d}-\frac{b^2}{r^2}\ln\frac{a}{d}\right]$$

(11)

$$M_r = \frac{W}{4\pi}(1+v)\left(\frac{a^2}{a^2-b^2}\right)\left\{\frac{1}{2}\left(\frac{1-v}{1+v}\right)\left[\left(1-\frac{d^2}{a^2}\right)\left(1+\frac{a^2}{r^2}\right)\right.\right.$$
$$\left.\left.-\left(1-\frac{r^2}{a^2}\right)\left(\frac{a^2}{r^2}-\frac{b^2}{r^2}\right)\right]\right\}$$

(12)

Then the radial, $\sigma_{r,\text{bend}}$, and circumferential, $\sigma_{c,\text{bend}}$, bending stress profiles are described as:

$$\sigma_{r,\text{bend}}(r) = \frac{6M_r(r)}{th_e^2}$$

(13)

$$\sigma_{c,\text{bend}}(r) = \frac{6M_c(r)}{th_e^2}$$

(14)

The maximum equivalent stress is then calculated by superimposing the centrifugal and bending stresses and using the von Mises criterion. As the maximum stress occurs at the inner radius, it is assumed that the stress concentrations induced by minor design features near the outer radius (i.e. the pin system, O-ring seal glands, and gas charging holes) do not affect the structural integrity of the end cap. The pocket for the retainers also makes the uniform thickness assumption somewhat of a simplification. These assumptions, as well as those inherent in plate theory, have been validated using FEA (Strohmaier 2014).

The piston separates the compressed gas from the hydraulic oil. Smooth translation is ensured by selecting a bearing ratio, defined as the length of the bearing divided by the diameter (Norton 2008), of greater than 1.5. Since the axle is selected as the bearing surface, the piston is designed with an L-shaped cross-section, which can be seen in Figure 1. While the face of the piston is subject to some bending loads, its thickness is driven by the axial length of commercially available piston seals. Due to their high strength to weight ratio, 6061-T6 and 7075-T6 aluminum are chosen for the end caps and piston, respectively.

3.3. Housing

Filament wound carbon fiber composite is used as the housing material for its high strength to density ratio. A circumferential fiber orientation is used, since this results in the maximum achievable circumferential tensile strength. In a flywheel rotor, the peak circumferential stress due to centrifugation is generally several times greater than the peak radial stress, but because of the anisotropic properties of the composite material, the failure mode due to tensile delamination in the radial direction must also be investigated.

Many methods have been proposed to address the issue of radial tension in a composite rotor. Nearly all approaches hinge on the fact that, in general, a composite material has a higher transverse compressive strength than transverse tensile strength (Kyu Ha et al. 2001). Some proposed methods induce a residual compressive radial stress during manufacturing or assembly, while others create rotor mechanical properties that vary in the radial direction. Fortunately, the construction of the HFA housing and the loadings to which it is exposed during operation provide a natural solution to the issue of radial tension. The higher density and compliance of the metal liner in conjunction with the fluid pressure acting on the liner provide radial compression at the inner radius of the composite wrap to counteract the radial tension due to centrifugal force. Because of their complex implications on mass, stress, energy capacity, and efficiency, the liner and wrap thicknesses are treated as design variables.

At non-zero angular velocity, the internal wall pressures on the gas and oil sides of the HFA are generally unequal. However, this difference is small enough to be neglected for the expected HFA operating speeds. To be conservative in estimating the housing stresses, the oil side pressure is used. Methods presented by Arnold et al. (2002) are employed to model the radial and

circumferential stresses in the liner-composite system. The analysis is based on the radial stress and displacement compatibility conditions at the interface between the liner and the wrap. All loads other than centrifugal force and internal pressure are assumed to contribute negligibly to stresses in the housing. There are three possible worst-case loadings: (1) depressurized at maximum angular velocity, for which the failure mechanism is composite delamination, (2) rated pressure at zero angular velocity, for which the failure mechanism is composite compressive failure, and (3) maximum pressure at maximum angular velocity, for which the failure mechanism is tensile hoop failure of the liner. For each of these cases, the liner safety factor is calculated using the von Mises criterion, and the wrap safety factor is calculated using the Tsai-Hill criterion (Staab 1999). Due to its high strength and galling resistance, AISI 4140 steel is chosen for the housing liner.

3.4. Bearing selection

The radial load on the bearings is due solely to eccentric force and is therefore greatest when $\omega = \omega_{max}$ and the oil volume is at its maximum. It is assumed that the specifications of the rotor balancing standard ISO 1940 can be met in the manufacture of the HFA (Bhushan 2002, ISO 2003). To mitigate uncertainty in this assumption, a safety factor of 10 is applied to the radius of eccentricity in the calculation of maximum radial load. Though it is taken into account in bearing selection, the net axial load on either bearing tends to be much smaller than the radial load, given the previously mentioned counteracting relationship between the HFA mass and the hydraulic system pressure.

For simplicity in sourcing the bearings, the gas and oil side shafts are chosen to have the same outer diameter. This diameter is chosen to accommodate the peak radial load on the bearings. Because of their low friction, minimal coefficient of thermal expansion, and ability to handle significant radial and axial loads, angular contact hybrid-ceramic ball bearings are chosen. While hybrid-ceramic bearings may necessitate increased resilience in the HFA mounting, they are more suitable for the high speeds at which the benefits of an HFA are most pronounced.

4. Energy loss mechanisms

The sources of energy loss in the HFA can be generally categorized into those which decrease the stored pneumatic energy and those which decrease the stored kinetic energy. Proper understanding of these loss mechanisms is essential to designing and optimizing the HFA. This section summarizes the methods used to model energy losses in the HFA.

4.1. Bearing and aerodynamic drag

Following procedures in commercial literature (NSK Motion and Control 2013), the frictional torque in a single ceramic angular contact ball bearing, T_b, can be estimated as:

$$T_b = \frac{\mu_b F_r d_{b,i}}{2} \quad (15)$$

where μ_b is an empirical frictional torque coefficient, F_r is the radial load on the bearing, and $d_{b,i}$ is the bearing inner diameter (shaft diameter). Whereas safety is the main concern in sizing the bearings and axle shafts, accuracy of predicted energy losses is most important in modeling bearing drag. For this reason, the actual expected radius of eccentricity, r_{ecc}, with no safety factor, is used to estimate bearing losses (ISO 2003). The total power dissipation due to friction in both bearings is then:

$$\dot{W}_b = 2\omega T_b = \frac{\mu_b(m + m_o)\omega^3 r_{ecc} d_{b,i}}{2} \quad (16)$$

where m is the mass of the solid HFA components and m_o is the maximum expected mass of the oil. The friction coefficient is estimated to be $\mu_b = 0.001$, which, is conservatively high for ceramic angular contact ball bearings (Stoneburner 2005, NTN 2009).

Methods presented by Genta (1985) are used to characterize the rate of energy dissipation due to aerodynamic drag, $\dot{W}_w$, on the HFA as:

$$\dot{W}_w = C_m \rho_{ch} \omega^3 r_o^4 \left(r_o + \frac{5}{2} l_h\right) \quad (17)$$

where ρ_{ch} is the density of the gas in the containment chamber, and the moment coefficient, C_m, is a function of the Reynolds number and the Knudsen number. The method of calculating the moment coefficient varies with Knudsen number, K_n, and Reynolds number, R_e, but for example, can be calculated for a laminar boundary layer and Knudsen number of $K_n \ll 1$ as

$$C_m = 3.87 R_e^{-1/2} \quad (18)$$

Losses in the hydraulic lines and valves are neglected for this study since such losses will should not be dominant and are highly dependent on the system in which the HFA is applied.

4.2. Storage pump-motor losses

Losses incurred by the storage PM are heavily dependent on the machine architecture. An axial piston architecture is selected for the HFA, as it is one of the most common hydraulic pump-motor architectures. Commercially-available aerospace axial piston pump-motors are capable of very high operating speeds (Vickers Fluid Systems 2000), which allows the storage PM to be directly coupled to the HFA.

The two primary loss mechanisms in hydraulic pumps and motors are due to volumetric and mechanical efficiencies, η_v and η_m, respectively. The PM losses, $\dot{W}_{PM}$, are

$$\dot{W}_{PM} = \dot{W}_{PM,in}(1 - \eta_v \eta_m) \qquad (19)$$

where the input power to the PM, $\dot{W}_{PM,in}$, is hydraulic power in motoring or mechanical shaft power in pumping. Volumetric and mechanical efficiencies in pumping are characterized using the McCandlish and Dorey models (McCandlish and Dorey 1984, Pourmovahed *et al.* 1992a):

$$\eta_v = 1e\frac{C_s}{xS} - \frac{P_s}{\beta_o} - \frac{C_{st}}{x\sigma} \qquad (20)$$

$$\eta_m = \frac{1}{1 + \frac{C_v S}{x} + \frac{C_f}{x} + C_h x^2 \sigma^2} \qquad (21)$$

where x is the fractional displacement position, the subscripted C parameters are loss coefficients, and the dimensionless parameters S and σ are defined as

$$S = \frac{\mu_o \omega}{P_s} \qquad (22)$$

$$\sigma = \omega D^{\frac{1}{3}}\left[2\frac{P_s}{\rho_o}\right]^{-\frac{1}{2}} \qquad (23)$$

While the loss coefficients in Equations (20) and (21) are typically determined experimentally for an existing machine, this study uses a single set of coefficients to characterize the entire range of PM sizes observed in a design optimization. The coefficients used are taken from manufacturer's data for a Rexroth A2V pump with a displacement $D = 107$ cm^3/rev (Pourmovahed *et al.* 1992b), as shown in Table 1.

4.3. Losses related to the HSRU

The HSRU has three primary loss mechanisms: flow losses in the axle ports, $\dot{W}_a$, leakage through the non-contacting seal, $\dot{W}_l$, and viscous friction in the non-contacting seal, $\dot{W}_{vh}$. The pressure drop in the axle ports is modeled using fully-developed duct flow theory. The laminar friction factor correlations used in this calculation take into account the hydrodynamic development length, as well as entrance and exit losses.

The annular leakage in the non-contacting circumferential seal is modeled using annular Poiseuille flow, and

Table 1. Manufacturer characterization of Rexroth A2 V pump-motor.

C_s	Laminar coefficient of slip	4.26×10^{-9}
C_{st}	Turbulent coefficient of slip	0
C_v	Coefficient of viscous drag	2.35×10^4
C_f	Coefficient of friction	5.37×10^{-2}
C_h	Hydrodynamic loss coefficient	53.6

the viscous friction in the seal is modeled using annular Couette flow. These flow models help describe the energy loss tradeoffs associated with the seal clearance and length. Larger seal clearances reduce viscous dissipation by reducing the shear flow gradient, but they also allow for more leakage by reducing axial flow resistance. Conversely, longer seal lengths reduce leakage but result in higher viscous dissipation. Because the diameter of the axle port scales with the clearance seal diameter, using larger axle diameters reduces axle port losses.

4.4. Other losses

The internal viscous dissipation, $\dot{W}_v$, which occurs as a result of velocity gradients in the rotating oil volume, is by far the most complex energy loss mechanism. The three-dimensional flows that occur during angular accelerations have analytic solutions only for the simplest cases (Duck and Foster 2001). Since transient numerical solutions of the flow are too computationally expensive for use within an optimization, the viscous dissipation is estimated using a simple empirical correlation developed by the authors in a previous study (Strohmaier *et al.* 2014) . The primary conclusion of this study is that advective, rather than viscous, effects dominate angular acceleration events, allowing for quick and efficient fluid angular velocity changes. Viscous dissipation depends on the angular acceleration rate, as well as absolute angular velocity, but it tends to be much lower than the other forms of energy loss in the HFA.

The energy required to establish and maintain a partial vacuum in the containment chamber is considered a parasitic draw. The vacuum chamber pressure is assumed to be maintained just above the oil vapor pressure. A simple model (Genta 1985), consisting of a vacuum pump with perfect mechanical efficiency at constant pumping speed S_p and adiabatic compression, is used to approximate the power required to maintain vacuum, $\dot{W}_{vac}$, as

$$\dot{W}_{vac} = \frac{\gamma}{\gamma - 1} S_p P_{ch}\left[\left(\frac{P_{amb}}{P_{ch}}\right)^{\frac{\gamma-1}{\gamma}} - 1\right] \qquad (24)$$

where the ratio of specific heats of air is $\gamma = 1.4$, P_{amb} is ambient pressure, and P_{ch} is vacuum chamber pressure. The effect of any air entrained or dissolved in the HSRU leakage is neglected for this study.

Energy losses due to fluid compressibility and sliding friction at the piston seals are not modeled in the present research, since they tend to be insignificant compared to other losses and do not significantly affect the dynamics of the HFA. The gas compression and expansion is assumed to occur isothermally and therefore is lossless. As the traction PM is not a component of the HFA, its losses are not considered in this analysis.

4.5. Drive cycle simulation

To evaluate the various mechanical stresses and energy losses, the HFA must be modeled in operation. For this

purpose, the HFA is assumed to be the sole energy storage mechanism in a series hydraulic hybrid mid-size passenger vehicle. The vehicle operates in a charge-depleting mode as it completes the Urban Dynamometer Driving Schedule (Environmental Protection Agency 2013), a well-known, widely-used drive cycle. Methods presented by Gillespie (Gillespie 1992) are used to model the components of road load. The time-varying tractive power profile, $\dot{W}_t(t)$, of the drive cycle is expressed as:

$$\dot{W}_t(t) = -(m_v + m)\left(\frac{dv}{dt} + f_r g\right)v - \frac{1}{2}\rho_{atm}v^3 C_D A_f \quad (25)$$

where m is the mass of the HFA system, v is the velocity of the vehicle, and ρ_{atm} is the density of the atmospheric air. The remaining vehicle parameters in Equation (25) are defined in Table 2, and their values have been chosen to reflect a typical mid-size passenger sedan. The initial conditions of the drive cycle are chosen such that the HFA is at a steady-state (fluid in rigid body rotation) and a full state of charge.

4.6. Control strategy and pump-motor selection

Prior to drive cycle simulation, a control strategy must be devised to allocate tractive and regenerative power between the kinetic and pneumatic domains in such a way that efficiency is maximized and pressure fluctuation is minimized. The large inherent losses of hydraulic pump-motors render the kinetic domain generally less efficient than the pneumatic domain.

While the system pressure could be held absolutely constant by using a variable displacement PM, this would require significant use of the kinetic domain and would incur high losses associated with low PM displacement. Instead, a simple "band control" method is selected. The idea behind band control is that higher drive cycle efficiency can be achieved by allowing some amount of system pressure fluctuation. A control fraction, $f_{control}$, defines a system pressure band of width $P_d f_{control}$, centered about a desired pressure, P_d, within which the control strategy defaults to using only the pneumatic domain. When the system pressure strays outside of this control band, the kinetic domain is activated, provided that its use will bring system pressure back towards the control band. This logic must be bypassed when the piston is at either extreme of its travel. In a real vehicle application, rapid activation and deactivation of the storage PM could lead to excessive noise, vibra-

tion and harshness. To reflect this concern, an upper limit is imposed on the frequency, f_{switch}, at which the control strategy can switch the kinetic domain on and off. The kinetic power demand is controlled through the use of a four-way valve that is capable of inverting the tank and pressure ports of the storage PM, in combination with a clutch to decouple the storage PM from the flywheel. As discussed earlier, this pump with have a very small displacement and a correspondingly small rotational inertia, which is therefore neglected. Since the system may require a rapid clutching frequency, future studies should include this noise, vibration, and harshness in the design parameters. A future study could also consider controlling motor speed immediately prior to clutching to reduce clutching losses. This study neglects this concern, along with the clutch cooling and inefficiencies in this valve and clutch system.

The ratio of the energy converted by the storage PM to the energy provided and absorbed purely within the pneumatic domain tends to be a good indicator of how well the control strategy promotes efficiency. This is called the usage ratio, R_u, and is defined as:

$$R_u = \frac{\int_t |\dot{W}_k| dt}{\int_t |\dot{W}_t|_{\dot{W}_k=0} dt} \quad (26)$$

where $\dot{W}_k$ is the power of the mechanical domain. The storage PM is sized to meet the maximum expected power demand during the cycle. From the known system pressure at every time step in the simulation, the traction PM displacement required to complete the drive cycle is calculated as:

$$D_t = \left|\frac{2\pi \dot{W}_t}{P_s \omega_t}\right|_{max} \quad (27)$$

where ω_t is the angular velocity of the traction PM. It is assumed that the vehicle differential has a 1:1 gear ratio, such that the traction PM angular velocity is a function of vehicle velocity, v, and tire diameter, d_t:

$$\omega_t = \frac{2v}{d_t} \quad (28)$$

Commercial data is used to approximate the mass of an axial piston storage PM as a function of displacement (Vickers Fluid Systems 2000).

$$m_{PM} = 0.236\left[kg/\frac{cc}{rev}\right]D + 1.12\,[kg] \quad (29)$$

The significance of the traction PM mass is discussed in the optimization section below.

5. Optimization

Having established the general design concept, along with mechanical stress and energy loss models, it is now possible to optimize the HFA for a hydraulic hybrid vehicle application. This section describes the methods by which such an optimization is carried out.

Table 2. Vehicle characteristics for drive cycle simulation, selected to represent a typical mid-size passenger Sedan.

Mass, m_v	1800 kg
Drag coefficient, C_D	0.3
Frontal area, A_f	2.3 m^2
Coefficient of rolling resistance, f_r	$9.0(10^{-3}) + 8.51(10^{-7})v^{2.5}$

There are seven geometric design variables: housing inner radius (r_i), housing outer radius (r_o), housing length (l_h), housing liner thickness (th_l), axle port diameter (d_i), HSRU seal clearance (c_s), and HSRU seal length (l_s). There are also two operational design variables: maximum allowable angular velocity (ω_{max}), and HFA charge pressure (P_c). A particular set of values for the nine design variables is referred to as a "design solution."

Bounds are placed on each of the design variables in order to prevent impractical or geometrically infeasible design solutions. In doing so, it is convenient to redefine a few of the design parameters. These redefinitions and the bounds for optimization are given in Table 3.

The HFA optimization has two objectives: minimizing system mass and minimizing energy losses over a drive cycle. System mass is defined as the sum of the mass of the HFA itself and the storage and traction PMs:

$$m_{sys} = m + m_{PM,s} + m_{PM,t} \qquad (30)$$

Defining system mass in this way allows a design solution to be judged not only by the mass-efficiency of its stored energy, but also by its ability to minimize system pressure fluctuation (Recall that smaller fluctuations in system pressure allow for a smaller traction PM).

The drive cycle loss, W_{loss}, is calculated as the time-integral of the sum of all power dissipation mechanisms during a drive cycle, plus a vacuum pumping energy consumption term:

$$W_{loss} = \int_{t=0}^{t_{dc}} \left[\dot{W}_v + \dot{W}_{vh} + \dot{W}_w + \dot{W}_b + \dot{W}_{PM} + \dot{W}_l + \dot{W}_a \right] dt + W_{vac}$$

$$(31)$$

The optimization is subject to two constraints. First, the mechanical stress safety factor on all components must be greater than three. Second, the energy stored must be sufficient to allow the vehicle to complete one full drive cycle. The NSGAII, an elitist genetic optimization algorithm, is used to find a set of Pareto-optimal (PO) design solutions (Deb *et al.* 2002). Table 4 summarizes the optimization problem and parameters of the solution algorithm.

Table 4. Summary of the genetic algorithm parameters.

# Design parameters	9
# Objectives	2
# Constraints	2
# Generations	400
# Individuals	200
Binary precision (bits)	7

6. Vehicle-scale optimization results

In analyzing the optimization results, it is useful to define two additional metrics to complement the design objectives. Drive cycle efficiency is defined using the energy losses during a drive cycle as a proportion of the cumulative energy conversion at the HFA.

$$\eta = 1 - \frac{W_{loss}}{\int_t |\dot{W}_t| dt + W_{loss}} \qquad (32)$$

The energy density, u_d, of a HFA solution is calculated as the amount of energy stored (at full SOC), E_d, per unit mass of the energy storage system.

$$u_d = \frac{E_d}{m + m_{PM,s}} \qquad (33)$$

Note that, because it is not actually a part of the energy storage system, the mass of the traction PM is excluded from the energy density calculation.

The high-level result of the HFA design optimization, a PO front of solutions, is shown in Figure 3. The most fundamental observation available from the PO front is that there is, as expected, a tradeoff between system mass and drive cycle energy losses. From the shape of the curve, it is clear that there are diminishing returns on pursuing either objective; the lower the mass, the higher the marginal penalty in losses. While the PO front does not explicitly reveal anything about design parameter values, the following is generally true. Solutions near the upper-left end of the PO front approach disk-style pure kinetic flywheels, characterized by short housings, small inner radii, thick walls, high maximum angular velocities, higher energy densities, and lower efficiencies. Conversely, solutions near the lower-right more closely resemble static hydraulic accumulators, with long

Table 3. Redefined design solution, used for the purposes of a design optimization.

Variable	Symbol	Translation	Lower bound	Upper bound	Units
Housing outer radius	r_o	–	1	[app. specific]	cm
Thickness fraction	f_{th}	$f_{th} = r_i/r_o$	1	[app. specific]	cm
Liner fraction	f_l	$f_l = th_l/(r_o - r_i)$	0	0.95	–
Inner length	l_i	$l_i = l_h - 2th_e$	0	0.1	–
Port diameter fraction	$f_{d,i}$	$f_{d,i} = d_i/(2r_i)$	0	0.5	–
HSRU seal clearance	c_s	–	0.5	50	mm
HSRU seal length	l_s	–	10	30	μm
Maximum angular velocity	ω_{max}	–	314	1,885	rad/s
Charge fraction	f_c	$f_c = P_c/P_d$	0.35	1	–

Figure 3. Pareto optimal front of solutions.

Figure 4. Energy capacity in the pneumatic and kinetic domains as a function of system mass for the Pareto-optimal (PO) set.
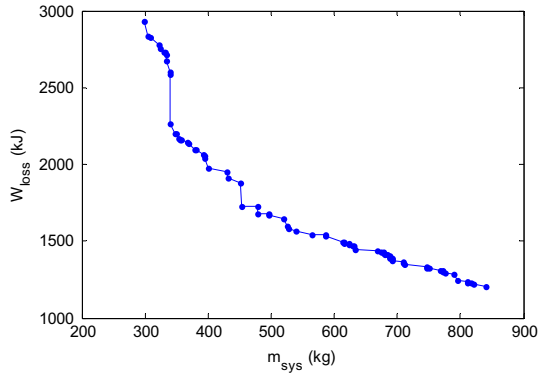
housings, large inner radii, thin walls, low maximum angular velocities, lower energy densities, and higher efficiencies. The PO front contains solutions with energy densities ranging from 7.47 to 31.6 kJ/kg and efficiencies ranging from 90.8 to 76.6%.

The flywheel-like solutions achieve low system masses because they have small geometric dimensions. Small dimensions generally correlate to low inertia, so these solutions must operate at high angular velocities in order to store sufficient energy. The high energy density of the flywheel-like solutions comes with a penalty of high drive cycle losses, since bearing drag, HSRU viscous loss, aerodynamic drag, and storage PM losses are all a function of angular velocity. The latter two loss mechanisms are particularly severe for the flywheel-like solutions, as their dependence on angular velocity is higher-order.

Moving towards the accumulator-like extreme of the PO set, design solutions maintain sufficient energy capacity through the growth of their dimensions. In effect, angular velocity is exchanged for inertia, which serves to maintain a reasonably high energy capacity in the kinetic domain. As shown by Equation (17), the aerodynamic drag torque has a fifth-order dependence on the outer radius of the housing (although this is slightly offset by the modest dependence of the moment coefficient on outer radius). To achieve higher efficiency with increased inertia, the housing length is increased rather than outer radius, because of the smaller aerodynamic penalty it incurs.

The accumulator-like designs exhibit lower usage ratios, as defined in Equation (26), since supply and demand of energy is more frequently met purely by using the pneumatic domain. These trends are perhaps best illustrated in the relationship between the kinetic and pneumatic storage capacities, shown in Figure 4, plotted against system mass.

It is worthwhile to examine the factors which limit the expanse of the PO front. For accumulator-like solutions, the housing inner length reaches its upper bound of 1.5 m. If the vehicle packaging constraints were lifted, drive cycle losses could continue to be reduced below
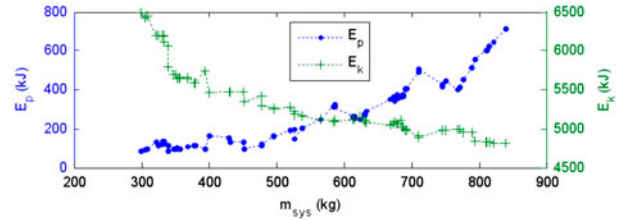
the best values observed in the optimization results. For the flywheel-like solutions, in contrast, none of the design parameters reach their bounds. This indicates that physical phenomena are acting to limit the expanse of the PO front. To further decrease the mass of the solutions at the high energy density end (i.e. to push solutions to be even more like flywheels), the optimization trends would suggest reducing the geometric parameters and increasing the angular velocity. Doing so, however, decreases the pneumatic energy and power capacities to unacceptably small values.

6.1. *Contextualizing the optimization results*

Having discussed the performance capabilities of the optimized HFA designs, it is now important to provide context for these capabilities. State-of-the art static hydraulic accumulators were said to be capable of about 6 kJ/kg energy storage density (Pourmovahed *et al.* 1988). However, optimizing the energy storage density of a static accumulator using the same architecture as the HFA provides a more direct assessment of how progressive the HFA concept actually is. A purely hydro-pneumatic accumulator with the same geometry and safety factor as the HFA results in an optimized energy density of 1.2 kJ/kg. To compensate for the fact that the selected HFA architecture may be suboptimal for a hydro-pneumatic accumulator, the hydro-pneumatic accumulator was also optimized while neglecting the mass of the axle and assuming a safety factor of one, resulting in an energy density of 5.1 kJ/kg. The highest density HFA design solution presented above provides six times this conservative energy density.

From the perspective of energy density (energy losses were not considered in the hydro-pneumatic accumulator optimization), the HFA clearly offers a significant benefit over traditional means of hydraulic energy storage. This optimization of a hydro-pneumatic accumulator resulted in a large aspect ratio for the highest energy density designs. Interestingly, flywheels follow nearly the opposite trend. Consider the simplest possible flywheel model, where the rotor is a simple, hollow cylinder of mass m and inner and outer radii of r_i and r_o, respectively. The energy density is:

$$u_d = \frac{\frac{1}{2}I\omega^2}{m} = \frac{\frac{1}{2}m(r_o^2 - r_i^2)\omega^2}{m} = \frac{1}{2}(r_o^2 - r_i^2)\omega^2 \qquad (34)$$

Equation (34) illustrates that energy density increases with the radial dimensions and is completely insensitive to the length of the rotor. An equivalent statement that takes into consideration the full HFA architecture is cumbersome to derive and analyze. However, it is easy to defend the general statement that kinetic energy storage increases with the fourth power of radial dimensions while mass increases with only the square of radial dimensions.

6.2. Selection of a design solution

Since the primary goal of HFA design is to increase the energy storage density, the design solution should represent significant improvement over the energy storage density of traditional accumulator storage, which is liberally estimated to be 5.1 kJ/kg for the given spatial constraints. Further insight into the design choice can be gained by considering the specific case of a mobile hydraulic system in a hydraulic hybrid vehicle. Recall that as the mass and energy losses incurred by a vehicle energy storage system increase, so does the energy required to complete a drive cycle, W_{dc}. In the present methods of simulation and optimization, each solution has been allowed to begin the drive cycle at full SOC (i.e. at its design energy capacity, E_d). The interaction between the mass-minimization objective and the constraint on unfinished distance results in each PO solution being fully-depleted by the end of the drive cycle, having stored just enough energy to complete it. Therefore, $W_{dc} \cong E_d$ for the purposes of the present discussion.

It is important to understand that, due to the range of HFA masses and losses, there is significant variation in the drive cycle energy, and therefore the design energy capacity, of the solutions in the PO set. In selecting a
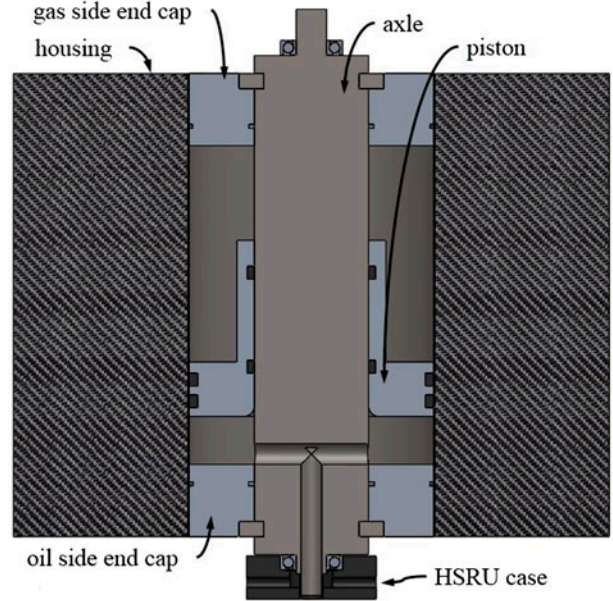

Figure 6.   Cutaway view illustrating solution 1.

particular solution from the PO set for a final design, E_d is arguably the most important metric. This is the amount of energy that must be "paid for," in the cost of energy and in green house gas emissions. Figure 5 shows the design energy capacities and system masses of the PO set, plotted against energy density.

Figure 5 illustrates an important trend in the PO results. Beginning with the most accumulator-like solutions (the far-left of this plot), increasing energy density of the HFA allows the design energy capacity to decrease. This is primarily due to the fact that a vehicle with a lower-mass energy storage system incurs less rolling resistance. However, at a certain point (near 10 kJ/kg), increases in energy density cease to pay off, at least
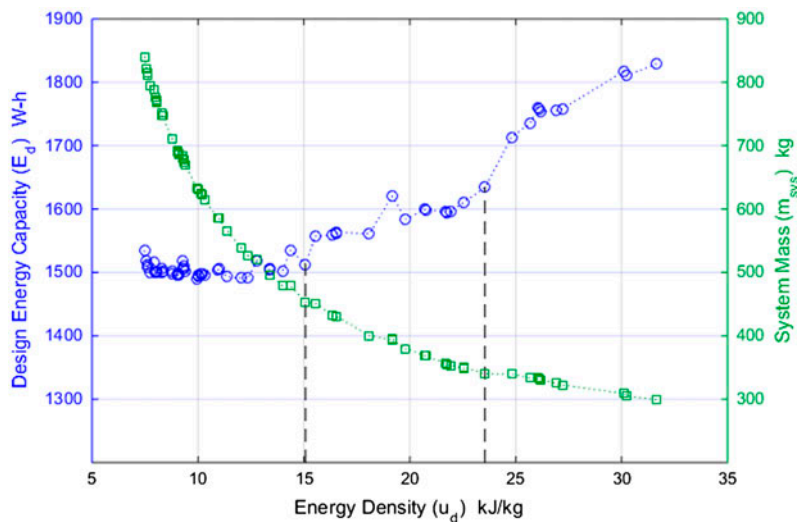

Figure 5.   Energy capacity and system mass vs. energy density for the PO set.

Table 5. Design variable values for two example HFA design solutions.

	Solution 1	Solution 2
Housing inner radius, r_i	14.14 cm	11.65 cm
Housing outer radius, r_o	34.43 cm	28.35 cm
Housing length, l_h	53.49 cm	54.75 cm
Housing liner thickness, th_l	0.157 mm	0.129 mm
Axle port diameter, d_i	24.12 mm	21.67 mm
HSRU seal clearance, c_s	10.47 micro	10.47 micro
HSRU seal length, l_s	2.42 mm	3.19 mm
Maximum angular velocity, ω_{max}	752.5 rad/s	1142.2 rad/s
Charge pressure, P_c	16.38 Mpa	16.06 Mpa
System mass, m_{sys}	453.0 kg	339.8 kg
Energy density, u_d	15.08 kJ/kg	23.55 kJ/kg
Energy capacity, E_d	1.898 kW-h	2.223 kW-h
Mass, excluding PMs	447.3 kg	335.8 kg
Capacity ratio, R_c	53.6	64.8
Housing safety factor	5.84	4.67
Storage PM displacement, D	19.6 cc/rev	12.27 cc/rev
Drive cycle losses, W_{loss}	1649.1 kJ	2064.3 kJ
Drive cycle efficiency, η	85.6%	81.2%
Usage ratio, R_u	1.96	2.09

Table 6. List of variables, English alphabet.

C_m	Aerodynamic moment coefficient
c_s	Circumferential seal clearance
D	Maximum pump-motor displacement
$d_{b,i}$	Bearing inner diameter
d_i	Axle inner diameter
d_s	Circumferential seal diameter
d_t	Vehicle tire diameter
E	Stored energy
E_a	Axle modulus of elasticity
E_d	Energy expended in a drive cycle
E_k	Stored kinetic energy
E_p	Stored pneumatic energy
F_a	Axial force in axle
$f_{control}$	Control fraction used by the control strategy
f_l	Liner thickness fraction
$f_{pressure}$	Pressure fraction to characterize observed pressure fluctuation
f_{switch}	Maximum allowable switching frequency for kinetic domain
F_t	Tractive force
f_{th}	Thickness fraction for housing wall
g	Acceleration of gravity
I_f	Equivalent moment of inertia, fluid components
I_s	Moment of inertia, solid components
k_s	Wave spring constant
l_h	Housing length
l_i	Housing inner length
l_p	Length of piston bearing section
l_s	Circumferential seal length
m	Mass, generic
M_c	Circular plate circumferential bending moment profile
m_h	Housing mass
m_o	Mass of oil volume
$m_{PM,s}$	Storage pump-motor mass
$m_{PM,t}$	Traction pump-motor mass
M_r	Circular plate radial bending moment profile
N_{ss}	Number of shoulder screws used in pin system
P_c	Gas charge pressure
P_d	Hydraulic system pressure, design

(Continued)

P_o	Oil pressure distribution
P_s	Hydraulic system pressure, actual
r	Radial position
r_a	Axle radius
R_c	Capacity ratio
r_{ecc}	Radius of eccentricity
r_i	Housing inner radius
r_o	Housing outer radius
R_u	Control strategy usage ratio
t	Time
T	Storage pump-motor torque
T_b	Bearing frictional torque
T_w	Aerodynamic torque
th_e	End cap thickness
th_l	Liner thickness
v	Drive cycle velocity in m/s
$\mathbb{V}_c$	Gas charge volume
v_{dc}	Drive cycle velocity in mph
$\mathbb{V}_g$	Instantaneous gas volume
$\dot{W}_t$	Tractive (total, road) power
$\dot{W}_a$	Axle throttling power dissipation
W_{dc}	Drive cycle energy
$\dot{W}_l$	Leakage power dissipation in high-speed rotary union
W_{loss}	Total energy losses
$\dot{W}_{PM}$	Storage pump-motor power dissipation
W_{vac}	Cumulative energy consumed by vacuum system
$\dot{W}_b$	Vacuum pumping power
$\dot{W}_{vh}$	Viscous power dissipation in high-speed rotary union
$\dot{W}_v$	Internal viscous power dissipation
$\dot{W}_w$	Aerodynamic (windage) power dissipation
x_o	Wave spring precompression

from the perspective of E_d. The higher operating speeds required by the most energy-dense solutions lead to larger drive cycle losses. To compensate, these solutions must actually have a higher energy capacity, even though the road loads continue to decrease with mass. The design with the lowest energy capacity for this scale PO set is located at 10 kJ/kg. As can be seen in Figure 5, a

Table 7.   List of variables, Greek alphabet.

δ_a	Axial elongation of the axle
η	Drive cycle efficiency
μ_b	Bearing friction coefficient
μ_{ch}	Dynamic viscosity of gas in the containment chamber
v	Poisson ratio
ρ	Density, generic
ρ_{ch}	Density of gas in the containment chamber
ρ_o	Oil density
$\sigma_{c,\text{bend}}$	Circular plate circumferential bending stress profile
$\sigma_{c,\text{cent}}$	Circumferential stress due to centrifugation
$\sigma_{r,\text{bend}}$	Circular plate radial bending stress profile
$\sigma_{r,\text{cent}}$	Radial stress due to centrifugation
ω	Angular velocity
$\omega_{\max}$	Maximum angular velocity
ω_t	Vehicle tire angular velocity

Table 8.   List of acronyms.

HFA	Hydraulic flywheel-accumulator
HSRU	High-speed rotary union
SOC	State-of-charge
PO	Pareto-optimal

small increase in energy capacity results in a 50% increase in energy density, up to 15 kJ/kg, resulting in an arguably better solution.

There are, of course, metrics other than E_d that should be considered in selecting a HFA design solution from a PO set (indeed, if the design energy capacity were the only important consideration, it would have been more appropriate to pose the optimization as single-objective, with the aim of minimizing E_d). For example, the lower-mass solutions tend to provide better vehicle handling, have a smaller packaging volume, and be less expensive to manufacture. For comparison purposes, a second design, located at the second vertical dashed line in Figure 5, is presented in Table 5. While both designs have low aspect ratios for convenient packaging, the first has higher drive cycle efficiency and the second has higher energy density. A cutaway view from a CAD model of the second design is shown in Figure 6. Notice that the optimization has driven the liner thickness of the selected design to a value of less than 0.2 mm. For the sake of practicality, this dimension is changed to 1 mm (Tables 5–8).

7.   Conclusion

This paper has described the hydraulic flywheel accumulator concept, as well as stress and energy models to aid in its design. Design optimization results indicate that, given the constraints imposed by a passenger vehicle-scale application, the HFA can achieve an energy density of more than 31 kJ/kg, operating at over 76% efficiency. Even with generous estimates of static accumulator energy density, this

represents at least a sixfold improvement in the energy storage density of hydraulic systems. Moreover, many design solutions are able to limit the fluctuation of system pressure to within a 10% band about the design pressure. This represents a distinct advantage over a traditional static accumulator, whose minimum SOC pressure may be as much as 63% lower than the design pressure (Tucker and Barth 2013), requiring significant over-sizing of the traction PM.

A pure flywheel offers higher energy storage density than the HFA while a traditional accumulator will provide higher power output. A system with energy stored in a physically separated flywheel and accumulator will also allow for a similar tradeoff in these attributes and allow the system pressure to be controlled independently of state of charge. The specific benefits provided by the HFA are found in the reduced volume achieved by placing the accumulator in the low energy density portion of the flywheel, the reduced manufacturing cost realized by the flywheel prestress provided by the fluid pressure, and the influence of the radial accumulator pressure profile on the system dynamics, specifically the fact that reducing kinetic state of charge and reducing pneumatic state of charge have opposite effects on pressure since slowing flywheel angular velocity reduces system pressure naturally.

Further research is required in order to validate the models used in the hydraulic flywheel accumulator design and optimization. Several assumptions and simplifications were made in the models, most prominently in the effect of internal fluid swirl, the effect of varying inertia of the flywheel at high speeds, and the effect of varying flywheel mass on the flywheel balance and vibration. The construction and testing of a prototype will allow for the exploration of these unknowns while providing a general proof of concept for the hydraulic flywheel accumulator.

Disclosure statement

No potential conflict of interest was reported by the authors.

References

Arnold, S.M., Saleeb, A.F., and Al-Zoubi, N.R., 2002. Deformation and life analysis of composite flywheel disk systems. *Composites part B: engineering*, 33, 433–459.

Bhushan, B., 2002. *Introduction to tribology.* Hoboken, NJ: Wiley.

Deb, K. *et al.*, 2002. A fast and elitist multiobjective genetic algorithm: NSGA-II. *IEEE transactions on evolutionary computation*, 6 (2), 182–197.

Duck, P. and Foster, M.R., 2001. Spin-up of homogeneous and stratified fluids. *Annual review of fluid mechanics*, 33, 231–263.

Environmental Protection Agency, 2013. Dynamometer drive schedule. Available from: http://www.epa.gov/nvfel/test ing/dynamometer.htm [Accessed 1 January 2015].

Environmental Protection Agency, 2015. Hydraulic hybrid research. *Clean automotive technology.* Available from: http://archive.epa.gov/otaq/technology/web/html/research-hhvs.html [Accessed 31 August 2015].

Exxon Mobil, 2008. Mobil DTE 25. *Material safety data sheet*, 1–8. Available from: http://mcos.com/assets/MobilD TE25MSDS.pdf [Accessed 1 January 2015].

Filipi, Z., *et al.*, 2004. Combined optimisation of design and power management of the hydraulic hybrid propulsion system for the 6×6 medium truck. *International journal of heavy vehicle systems*, 11 (3/4), 372–402.

Genta, G., 1985. *Kinetic energy storage: theory and practice of advanced flywheel systems*. London: Butterworth & Co.

Gillespie, T.D., 1992. *Fundamentals of vehicle dynamics*. Warrendale, PA: Society of Automotive Engineers.

Heap, J.C., 1964. *Bending of circular plates under a uniform load on a concentric circle*. Lemont, IL: Argonne.

ISO, 2003. *ISO Standard 1940-1, Mechanical vibration- balance quality requirements for rotors in a constant (rigid) state - Part 1: Specifications and verification of balance tolerances.* http://www.dcma.mil/NPP/files/ISO_1940-1.pdf

Kyu Ha, S., Kim, D.J., and Sung, T.H., 2001. Optimum design of multi-ring composite flywheel rotor using a modified generalized plane strain assumption. *International journal of mechanical sciences*, 43, 993–1007.

Li, P.Y., Van de Ven, J.D. and Sancken, C., 2007. Open accumulator concept for compact fluid power energy storage. *Proceedings of IMECE*. Seattle, WA: American Society of Mechanical Engineering, 127–140.

McCandlish, D. and Dorey, R.E., 1984. The mathematical modelling of hydrostatic pumps and motors. *Proceedings of the institution of mechanical engineers, part B: management and engineering manufacture*, 198 (10), 165–174.

Norton, R.L., 2008. *Design of machinery*. New York, NY: McGraw-Hill.

NSK Motion and Control, 2013. Rolling bearings CAT. No. E1102m. http://www.jp.nsk.com/app01/en/ctrg/index.cgi? rm=pdfView&pno=e1102m

NTN, 2009. Ball and roller bearings, CAT. No. A-1000-XI. http://www.ntnamericas.com/en/website/documents/brochures-and-literature/catalogs/ntn_a1000xi_ball_and_roller_bearings_lowres.pdf

Pedchenko, A. and Barth, E.J., 2009. Design and validation of a high energy density elastic accumulator using polyurethane. *ASME 2009 dynamic systems and control conference*, Vol. 1. Hollywood, CA: American Society of Mechanical Engineering, 283–290.

Perkins, W.G., 1973. Permeation and outgassing of vacuum materials. *Journal of vacuum science and technology*, 10, 543–556.

Pourmovahed, A., Beachley, N.H., and Fronczak, F.J., 1992a. Modeling of a hydraulic energy regeneration system: part I – analytical treatment. *Journal of dynamic systems, measurement, and control*, 114 (1), 155–159.

Pourmovahed, A., Beachley, N.H., and Fronczak, F.J., 1992b. Modeling of a hydraulic energy regeneration system: part II – experimental program. *Journal of dynamic systems, measurement, and control*, 114 (1), 160–165.

Pourmovahed, A., *et al.*, 1988. Experimental evaluation of hydraulic accumulator efficiency with and without elastomeric foam. *Journal of propulsion*, 4 (2), 185–192.

Staab, G.H., 1999. *Laminar composites*. Boston, MA: Butterworth-Heinemann.

Stoneburner, M., 2005. Power transmission/maintenance-hybrid ceramic bearings: More mettle than metal. *Plant Engineering*, 59 (8), 71–73.

Strohmaier, K.G., 2014. *Modeling, optimization, and detailed design of a hydraulic flywheel-accumulator*. Minneapolis, MN: University of Minnesota.

Strohmaier, K.G. *et al.*, 2014. Experimental studies of viscous loss in a hydraulic flywheel accumulator. *National Conference on Fluid Power, International Fluid Power Exposition*, March 4–8, 2014, Las Vegas, NV, 0369–000017.

Timoshenko, S. and Woinowsky-Krieger, S., 1959. *Theory of plates and shells*. 2nd ed. New York, NY: McGraw-Hill.

Tucker, J.M. and Barth, E.J., 2013. Design, fabrication, and evaluation of a distributed piston strain-energy accumulator. *International journal of fluid power*, 14, 47–56.

Van de Ven, J., 2009. Increasing hydraulic energy storage capacity: flywheel-accumulator. *International journal of fluid power*, 10 (3), 41–50.

Vickers Fluid Systems, 2000. "A descriptive summary of Vickers inline pumps and their applications," SE-103F. Jackson, MS: Copyright Eaton Aerospace.

Young, W.C. and Budynas, R.G., 2002. *Roark's formulas for stress and strain*. New York, NY: McGraw-Hill.